# Cross Fusion-Based Low Dynamic and Saturated Image Enhancement for Infrared Search and Tracking Systems

**BYEONG HAK KIM**[1,3], **CIRIL BOHAK**[2], **KI HOON KWON**[1], **AND MIN YOUNG KIM**[1,4]

[1]School of Electronics Engineering, Kyungpook National University, Daegu 41566, South Korea
[2]Faculty of Computer and Information Science, University of Ljubljana, 1501 Ljubljana, Slovenia
[3]Hanwha Systems Company, Gumi 39376, South Korea
[4]Research Center for Neurosurgical Robotic System, Kyungpook National University, Daegu 41566, South Korea

Corresponding author: Min Young Kim (minykim@knu.ac.kr)

**ABSTRACT** Unmanned aerial vehicles and battleships are equipped with the infrared search and tracking (IRST) systems for its mission to search and detect targets even in low visibility environments. However, infrared sensors are easily affected by diverse types of conditions, therefore most of IRST systems need to apply advanced contrast enhancement (CE) methods to cope with the low dynamic range of sensor output and image saturation. The general histogram equalization for infrared images has unwanted side effects such as low contrast expansion and saturation. Also, the local area processing for saturation reduction has been studied to solve the problems regarding the saturation and non-uniformity. We propose the cross fusion based adaptive contrast enhancement with three counter non-uniformity methods. We evaluate the proposed method and compare it with conventional CE methods using the discrete entropy, PSNR, SSIM, RMSE, and computation time indexes. We present the experimental results for images from various products using several datasets such as infrared, multi-spectral satellite, surveillance, general gray and color images, as well as video sequences. The results are compared using the integrated image quality measurement index and they show that the proposed method maintains its performance on various degraded datasets.

**INDEX TERMS** Infrared images, IRST, image enhancement, low dynamic, fusion, target detection.

## I. INTRODUCTION

Infrared search and tracking (IRST) systems are used on unmanned aerial vehicles (UAV) and surveillance applications such as pan-tilt searching electro-optical systems [1]. In such applications, it is required to process contrast expansion and noise reduction because of the low output characteristics of IR detection sensors and because its image dynamic range is severely degraded by low visibility conditions occurring due to light scattering by microscopic aerosols such as the fog and haze. In fact, several complaints of flight pilots have been reported about the difficulties associated with recognizing summit mountain lines (SML) or detecting targets due to low dynamic and saturated images of IR

The associate editor coordinating the review of this manuscript and approving it for publication was Claudio Cusano.

systems. The saturation phenomenon also poses problems in industrial, medical, and security camera systems as well as defense applications [2]. In recent days, many machine-learning and deep-learning based automatic target detection and object tracking models have been used to make the detection even more efficient and accurate [3]–[9]. The auto-detection and object tracking methods are affected by the quality and Homogeneous brightness of training images and are used to derive more information from the images with respect to how well they represent targets and details.

Traditionally, the general histogram equalization (GHE) is a popular solution to improve low dynamic contrast images based on histogram equalization (HE) calculations [10], [11]. The GHE method expands the contrast to the maximum dynamic range and offers an effective way for fast calculation. However, it produces locally saturated output images,
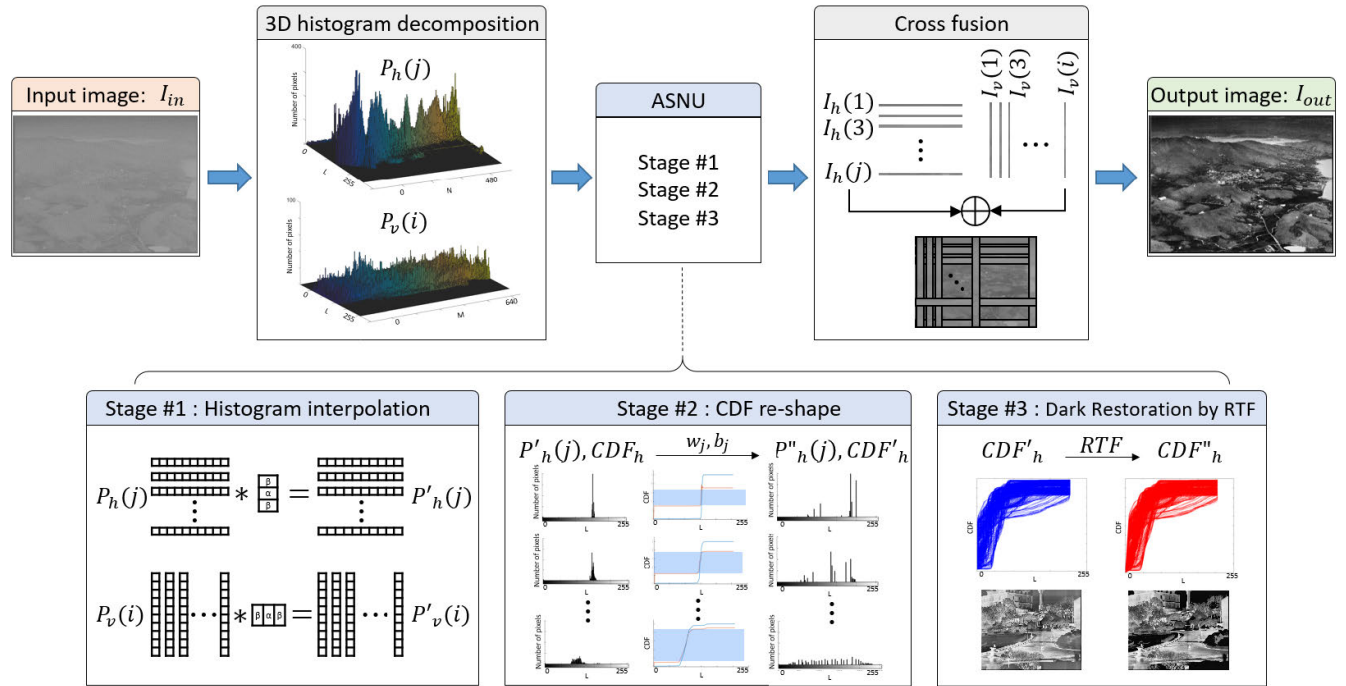
**FIGURE 1.** A conceptual flow chart of the proposed method.

degrades the target detection and the recognition performance [12]–[14].

Conversely, many studies have proposed solutions for overcoming the low dynamic and over-saturated image outputs by GHE. The brightness preserving bi-histogram equalization (BBHE) and particle swarm optimization (PSO) based local entropy weighted histogram equalization separates an original image histogram into two sub-histograms based on the mean value of the input image and performs HE using recombined two sub-histograms [15], [16]. The local area processing (LAP) based methods are applied to improve contrast for entire areas of images. The contrast limited adaptive histogram equalization (CLAHE) is a method based on LAP principle [17]. However, the decisions of optimal limit values and divided units are not easily fitted for various image characteristics. Furthermore, the dualistic sub-image histogram equalization (DSIHE) separates an image to equal two sub-images using the median value [18]. It focuses on maintaining image brightness quality after HE process, but it does not perform well in high contrast stretching.

The brightness preserving dynamic histogram equalization (BPDHE) uses, the local maxima of the smoothed histogram to divide the histogram into dynamic level ranges [19]. The authors of singular value decomposition discrete wavelet transform (SVD-DWT) method studied singular value based image equalization (SVE) [20]. These approaches are utilized to eliminate image saturation problems. However, the SVD-DWT method has little effect on the contrast expansion ratio and is computationally expensive.

Recently presented, transform based gamma correction (TGC) method uses an automatic transformation technique and an adaptive gamma correction with weighting distribution (AGCWD) to improve the brightness of dimmed images [21]. It offers great performance in comparison with other methods, however, it returns low contrast enhancement results for white-saturated images. The contrast enhancement algorithm based on gap adjustment for HE (CegaHE) adjusts the gaps between two gray levels using the adjustment equation [22]. The interlace histogram equalization (IHE) method uses a simple cross fusion method [23]. However, it shows severe non-uniformity problems for background image areas.

In this study, we propose a new, efficient contrast enhancement method with a high contrast expansion ratio, low noise output and fast computation time. This approach implements the concept of adaptive suppression of non-uniformity (ASNU) with the maximum spatial occupancy of the 3D histogram. The main concept of the proposed method is the image cross fusion (CF) on the output of ASNU stages. Fig. 1 shows the overall outline of the proposed method as a block diagram. In the first step, a low contrast input image $I_{in}$ is decomposed into $h + v$ units to be used in 3D histograms for probability distribution functions, $P_h(j)$, $P_v(i)$. Acquired 3D histograms enter three stages of the ASNU step before entering the final cross fusion step.

In the first stage of ASNU, the interpolation for decomposed neighboring histograms $P_h(j)$ and $P_v(i)$ is performed. In the second stage, the cumulative distribution function (CDF) of interpolated histograms $P'_h(j)$ and $P'_v(i)$ is adaptively re-shaped according to the image characteristics of

each histogram using $w_i$, $b_j$ parameters. In the third stage, the re-shaped $\text{CDF}'_h$ and $\text{CDF}'_v$ are passed through rational transfer function (RTF) filter for restoration of the dark and white pixel levels. Finally, as the output of ASNU, $\text{CDF}''_h(j)$ and $\text{CDF}''_v(j)$ are derived and delivered to the CF step. In the CF step, the $\text{CDF}''_h(j)$ and $\text{CDF}''_v(j)$ are mapped to the sub-image values $I_h$ and $I_v$ for the final CF output image $I_{\text{out}}$.

The experimental results show the CE images and their histograms obtained using selected methods and the proposed method which are compared with the images obtained using the IRST products from UAV systems. The visual assessment of performance shows which method is most suitable for efficient SML detection or target detection in conditions yielding low dynamic images. In addition, we present the resulting images and histograms from *Remote sensing*, *Surveillance*, *Grayscale*, and *RGB* datasets for an extended validation. In the results, we also show the performance of the methods on real-time video sequences where the image dynamic range is continuously changed from dark to white values with a narrow dynamic band. The results confirm which methods can be applied to real applications where the image dynamics change a lot. For quantitative measurement, the normalization index for time, entropy, PSNR, SSIM, and RMSE are presented in the comprehensive evaluation of experimental results.

In this work, we propose an effective contrast enhancement with low computational complexity and robust image quality. This approach is based on a concept of the image cross fusion with ASNU for a maximal spatial fill factor of 3D histograms.

## II. RELATED WORK
### A. LOW DYNAMIC AND SATURATION PROBLEMS
The most important role of an image signal processor for the IR image sensor is to increase the contrast ratio in the process of converting the detected photon energy from focal plane area of semiconductor sensors to a digital signal output. The Fig. 2(a) shows a result image after contrast enhancement method (CEM) and non-uniformity correction applied to the original input image shown in Fig. 2(b). In order to improve such low dynamic images, most advanced IR image sensors focus on the efficient CEM process. However, if IR images are acquired when moisture particles like a fog or haze are present in the environment, the output images are degraded substantially. As shown in Fig. 2(c), in such cases the white saturation phenomenon occurs due to the distribution of bright pixels, so the images are saturated to white levels. To solve these problems, we developed a method which improves the black and white low dynamic image and is at the same time computationally efficient.

### B. MOTIVATION
The main conceptual mathematics of the GHE method is represented by the following three simple equations:

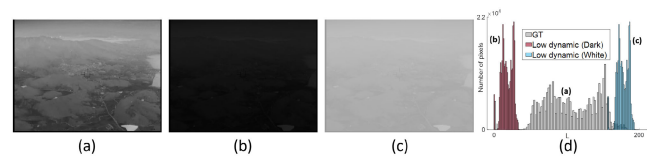$$\text{hist}(i) = \text{hist}(x = i) = \frac{n_i}{M \times N}, \quad 0 \le i < L, \quad (1)$$



**FIGURE 2.** Examples of low dynamic ranged images. (a) GT, (b) a low dynamic image(dark), (c) a low dynamic image(white).

where $L$ is the maximum value of intensity in the image (in the case of 8-bit image, the $L$ is 255). $M \times N$ is the total number of pixels in the $M \times N$ array, $n_i$ is the number of pixels with same intensity, and $\text{hist}(i)$ is normalized pixel value for $i$-th intensity level. The following equation 2 is used to calculate the cumulative distribution function (CDF) from the $\text{hist}(i)$:

$$\text{CDF}(i) = \sum_{i=0}^{L} \text{hist}(i), \quad (2)$$

where CDF is expressed as a graph of the $\text{hist}(i)$ accumulating in pixel order. The maximum value on the x-axis is L, and the maximum response value on the y-axis is 1.

$$I_{\text{GHE}} = \text{Int}(\frac{\text{CDF}(i) - 1}{M \times N} \times L). \quad (3)$$

Equations 1 to 3 define how the GHE method normalizes the histogram, accumulates it in the CDF, and distributes it uniformly. The GHE extends histograms which are concentrated in a narrow range to the entire range of the intensity. The GHE seemed to be the best countermeasure for low dynamic images, but it shows limitations such as low contrast resolution and image saturation problems [23].

As a more advanced method, the BBHE divides an image into two areas: (1) dark level of the histogram and (2) bright level of the histogram. It stretches the intensity values more effectively than the GHE method. As other LAP based methods, the CLAHE tries to enhance the image by using a local HE calculation as units of separated square sub-images. It shows the high contrast resolution and stretching effect, but it has a lot of noise and saturated image parts remains.

To overcome these limitations, the SVD-DWT, AGCWD, and CegaHE are studied. Methods try to solve over-stretching or under-stretching problems as well as high contrast enhancement effects [20]–[22]. However, the SVD-DWT is computationally very expensive due to the complex processes such as wavelet transform. In order to solve the aforementioned problems associated with the conventional 2D histogram equalization method, we analyze the 3D histogram using a method which decomposes the image into line units and tries to find the reasons for the fundamental problem of conventional methods. When a white-saturated image as shown in Fig. 3(a) is adjusted by the GHE method, the output is the Fig. 3(b). The histogram of the image is well stretched from the lowest intensity level to the highest intensity level using conventional 2D histogram analysis.

However, as a result of the 3D histogram, you can see that the pixel values are stretched to the whole range from
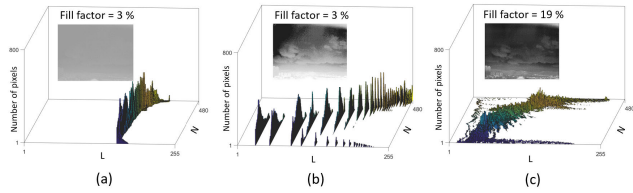
**FIGURE 3.** Fill-factors for 3D histograms. (a) Input (3%), (b) GHE (3%), (c) Proposed (19%).

**TABLE 1.** Fill factors on 3D histograms.

| Image | Original | GHE | CLAHE | AGCHE | Proposed |
|---|---|---|---|---|---|
| *IRST-UAV* | 18.4 | 16.8 | **27.8** | 17.7 | **49.2** |
| *City-sky* | 3.4 | 3.1 | **28.7** | 3.4 | **18.9** |
| *KNU-HQ* | 7.5 | 6.8 | **11.4** | 7.5 | **43.3** |

minimum to maximum pixel values, but the pixels that can be represented are not being used to widen the distributed areas. Fig. 3(c) shows an example of a 3D histogram using the proposed method, and it utilizes the pixels that can be represented in a wide pixel intensity range. We measure the grades of such pixel representation of the fill factor (FF), and the calculation of the FF are defined with equation 4. The FF are representing the ratio of the occupied area in 3D histogram space. Table 1 shows the FF result values for representative image data from the experimental dataset. The proposed method has advantages according to high FF value calculated by:

$$\text{Fill factor} = \left[ LN - \sum_{i=1}^{LN} \text{num}(hist_{3D}(i) = 0) \right] / LN, \quad (4)$$

where $L$ is the maximum intensity level (255), and $N$ is the number of lines obtained in the image decomposition process. $hist_{3D}(i)$ denotes the number of pixels in each sequence (i) in the entire 3D histogram area. Therefore, the equation 4 represents the filled levels of the region occupied by pixels with a value in the 3D histogram.

## III. METHODS
### A. THE CROSS FUSION PROCESS
An efficient and adaptive contrast enhancement method for low dynamic black and white saturated images, and the method for expressing the image in detail with maximum FF value, begins with a cross fusion (CF) process. This approach is motivated by the analysis of the 3D histogram and the 3D histogram is used for the CF process of the decomposed input images. As displayed in Fig. 4, the CF procedure starts from the decomposition of the input image (a) into line units in different directions as shown in (b) and (c). The aforementioned 3D histogram decomposition operation described in Fig. 1 is expressed by the following two equations:

$$P_h(j) = I_{in}(j)/M, \quad P_v(i) = I_{in}(i)/N. \quad (5)$$

The input image, $I_{in}$ decomposition in each line unit performs following $L$ and $M$ to the adaptive suppression of
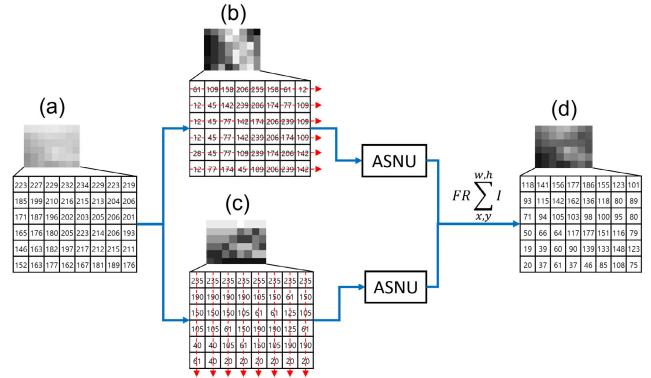


**FIGURE 4.** The basic principles for CF process. (a) An example of input image, (b) processes of horizontal direction, (c) processes of vertical direction, (d) an example output of CF process.

non-uniformity (ASNU) before the output image is recomposed by CF calculation.

The CF operation for the output image $I_{out}$ is implemented as a simple weighted sum define by:

$$I_{out} = \sum_{j=1}^{M} \sum_{i=1}^{N} FR \times (I_{h-ASNU} + I_{v-ASNU}) \quad (6)$$

The fusion ratio (*FR*) parameter for the typical quality of image improvement is 0.5. Depending on the system, *FR* can be adjusted if stronger or weaker stretching is required.

In successfully cross fused images, noise is amplified in the form of non-uniformity and overstretching due to the decomposition and re-synthesis of the image. To counter this we use ASNU method.

### B. ADAPTIVE SUPPRESSION OF NON-UNIFORMITY
#### 1) INTERPOLATION OF DECOMPOSED HISTOGRAMS (IDH)
The IDH process prevents the components that are decomposed in the line direction from being streaked with a sudden brightness distribution difference. An interpolation method is a representative method for preventing non-uniformity improvement or quantization phenomenon in the image. In general, the interpolation method is a direct image processing method of changing image pixel values and is used to softly fill empty pixels that need to be generated when enlarging an output image.

We use a modified interpolation concept in the IDH method to smoothly connect decomposed histograms.

We can improve the components of the histogram of each line $P_h(j)$ and $P_v(i)$ as an indirect improvement method for computationally less expensive implementation. In addition, we used bicubic interpolation curves to derive the interpolation functions $\phi_{h,v} = [\ \beta\ \alpha\ \beta\ ]$ in advance to enable fast computation:

$$P'_h(j) = \begin{bmatrix} P_h(j-1) \\ P_h(j+0) \\ P_h(j+1) \end{bmatrix} \times \phi_h, \quad P'_v(i) = \begin{bmatrix} P_v(i-1) \\ P_v(i+0) \\ P_v(i+1) \end{bmatrix} \times \phi_v$$
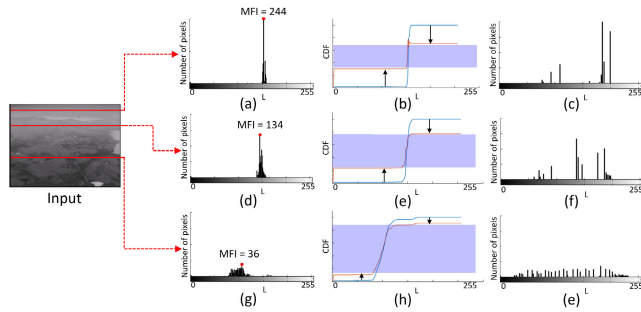
$$(7)$$

**FIGURE 5.** The basic principles for CDF reshaping. (a),(d), and (g) Examples of decomposed histograms, (b), (e), and (h) results of adaptive suppression, (c), (f), and (i) output histograms of CDF reshaping process.

### 2) CDF RESHAPING

This process is the second step of ASNU. The purpose of this step is to reduce the black and white noise that is generated as a result of expanding the uniform areas and does not require the contrast enhancement. The operation principle of CDF reshaping is shown in Fig. 5. First, the most frequent intensity (MFI), $m_j$ is detected in the input image for each decomposed component as shown in Fig. 5(a), (d), and (g) and is defined as:

$$m_j = \underset{x}{\text{argmax}}\, P_{h,x=1}^i(j). \tag{8}$$

The weight and bias parameters for CDF reshaping are calculated with equations 9 and 10 using the derived MFI parameters as $m_j$ and $m_i$.

$$w_j = 1 + m_j \times (1/MN), \quad b_j = (w_j - 1.0)/2w_j \tag{9}$$
$$w_i = 1 + m_i \times (1/MN), \quad b_i = (w_i - 1.0)/2w_i \tag{10}$$

Finally, CDF reshaping is performed as defined in equation 11 below. The computation of the vertically decomposed components is performed in a similar way.

$$\text{CDF}_h'(j) = \text{CDF}_h(j)/w_j + b_j \tag{11}$$

### 3) DARK AREA RESTORATION

The results of CDF reshaping according to $w$ and $b$ can be missing black and white components in the calculation of uniform image components. In addition, according to Weber's law, human vision has a high resolving power for levels close to dark gray [24]. Gamma correction is generally used to increase resolution for dark image components [25]. We use the rational transfer function (RTF) to compensate for the dark pixel area restoration. It works for mutual heterogeneity suppression of the decomposed images as well as restoring the dark pixel areas. In addition, the RTF filter achieves a low-pass filter effect, and thus provides dark area correction and produces smooth images. Furthermore, the RTF filter is simple and fast without complex processing. As such it, is suitable for real-time imaging sensor systems.

The basic formula of RTF is:

$$y(n) = \frac{1}{dL}\left[x(n) + x(n-1)\cdots + x(n-(dL-1))\right], \tag{12}$$
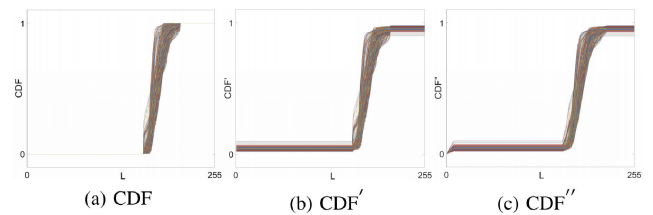
**FIGURE 6.** Results of CDF-reshaping and dark restoration. (a) Input CDF, (b) result by CDF-reshaping, (c) result after dark area restoration.

where the $dL$ is length of denominating terms. This equation can be applied for the CDF-reshaping as shown in:

$$\text{CDF}_h''(j) = \frac{1}{dL}[\text{CDF}_h'(j) + \text{CDF}_h'(j-1) + \cdots + \text{CDF}_h'(j-(dL-1))] \tag{13}$$

$\text{CDF}_h''(i)$ is also calculated in the same manner as defined by equation 13. $I_{h-\text{ASNU}}$ and $I_{v-\text{ASNU}}$ from the CDFs are calculated as shown in:

$$I_{h-\text{ASNU}} = \text{Int}(\frac{\text{CDF}_h'' - 1}{M} \times 255) \tag{14}$$
$$I_{v-\text{ASNU}} = \text{Int}(\frac{\text{CDF}_v'' - 1}{N} \times 255) \tag{15}$$

Fig. 6(a) shows an input CDF, Fig. 6(b) shows an intermediate CDF, and Fig. 6(c) shows a result using the CDF-reshaping processes. On the x-axes of three figures are pixel values, and on the y-axes are accumulated numbers for each value. The numbers of lines on one figure are N, where N is the number of divisions of the histogram. Fig. 6(a) shows the CDF before correction with the IDH procedure is performed on image components obtained by decomposing the image into N components. Fig. 6(b) shows the intermediate result in which CDF-reshaping is performed by the parameters $w_j$ and $b_j$ from Fig. 6(a). Here, we can derive improved $\text{CDF}'$ that adaptively suppress the non-uniformity due to amplifying the contrast ratio in uniform areas from CDF. The Fig. 6(c) is the result obtained using final reshaped CDF for dark area restoration and precision filtering by the RTF.

We have described the IHD, CDF-reshaping, and dark restoration processes defined by three stages of ASNU. The final outputs $I_{h-\text{ASNU}}$ and $I_{v-\text{ASNU}}$ of the process are output to the final image by performing the CF procedure according to equation 6.

## IV. EXPERIMENTAL RESULTS

In this section, we compare the results of methods: CLAHE, which is widely used for improving the contrast ratio in the regions as well as traditional methods such as GHE, BBHE, DSIHE, BPDHE, IHE, SVD-DWT, AGCWD, CegaHE, and the proposed method. The experimental results were obtained for images from five image datasets and a real-time video sequence dataset using 10 above-mentioned methods. The GHE is a representative method of processing the contrast

**TABLE 2.** Description of experimental datasets.

| Num. | IRST | Remote-Sensing | Surveillance | Grayscale | RGB |
|------|------|----------------|--------------|-----------|-----|
| 1 | IRST-UAV | Wave-01(Blue) | Cross-road | Stars | A girl |
| 2 | City-sky | Wave-02(Green) | Airport | Big-cat | Small-cat |
| 3 | KNU-HQ | Wave-03(Red) | Highway | Squirrel | Tree-APT |
| 4 | APT-sky | Wave-04(NIR) | Truck | Clouds | Squirrel |
| 5 | Drone | Wave-05(SWIR-I) | Tank | Structure | Monkey |
| 6 | GP-enter | Wave-06(SWIR-II) | - | An eye | Couple |
| 7 | GP-grass | Wave-07(PC) | - | Brain | Hazy |
| 8 | GP-park | Wave-08(Cirrus) | - | - | Startrack |
| 9 | Statue | Wave-09(TIRS-I) | - | - | - |
| 10 | Northgate | Wave-10(TIRS-II) | - | - | - |
| 11 | Pedestrian | - | - | - | - |
| 12 | Student | - | - | - | - |
| #1~2100 | Video**35(sec)** | - | - | - | - |

enhancement for many applications. Also, BBHE, CLAHE, IHE, DSIHE, BPDHE, SVD-DWT, AGCWD, CegaHE, and the proposed method are compared using visual assessment. In the related work section, we presented low dynamic images with black and white as shown in Fig. (2) (b) and (c). They are mostly caused by an insufficient or excessive amount of light in the scene. The experimental results were obtained for images listed in Table 2: IRST (12 images), Remote-Sensing (10 wavelengths) [26], Surveillance (5 images), Grayscale (7 images), and RGB (8 images). Also, IRST video sequence (#1 to #2100 frames) was used in the visual assessment.

In most cases, the ground truth images do not have appropriate light intensity properties. In the case of Remote-sensing satellite IR images, experimental input images are GT images. In other cases from in Fig. 7(a) to Fig.13 (a), the input images are generated as low dynamic images using GT images. The results are shown for multiple methods together.

For the verification of various IR applications including IRST, we show the results for several different images for security monitoring and surveillance using multi-spectral wavelength images. Since the results of the research, such as improvement of the image, are required to be verified for various cases, we were able to obtain outdoor observation images, such as cross-road, airport, highway, truck, and medical images. Because the results of research such as image improvement require a comparative verification of the data from various application fields, we show telescope images and medical images together with IRST, Surveillance, and Grayscale dataset results which were widely used in previous studies.

Finally, we also show the results of applying to RGB images, including a dataset named *A girl* to check whether the effect is applied to the degraded or hazy (white saturated) color image.

In the experimental section, the most representative images are selected from five datasets. The resulting images are shown together with their histograms. All the results including the remaining experimental images are shown in the supplemental materials.
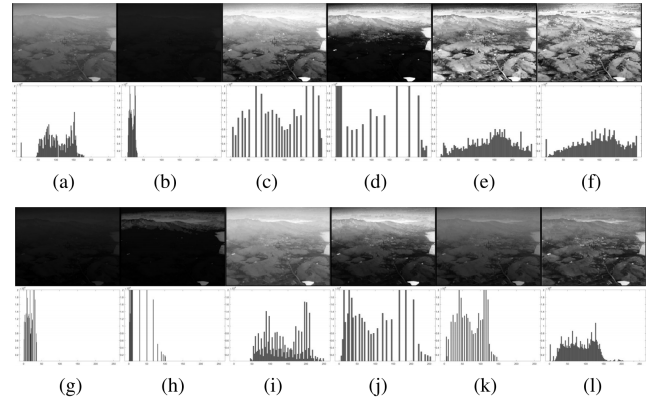


**FIGURE 7.** *IRST-UAV* dark low-dynamic image (upper rows: results of images, lower rows: results of histogram [x-axis: levels of intensity, y-axis: number of pixels]) (a) GT, (b) Input, (c) GHE, (d) BBHE, (e) CLAHE, (f) IHE, (g) DSIHE, (h) BPDHE, (i) SVD-DWT, (j) AGCWD, (k) CegaHE, (l) Proposed.

### A. VISUAL ASSESSMENT OF THE IRST DATASET

Fig. 7 shows the resulting images form the IRST dataset, in which the GT image Fig. 7(a) is compared with the results from different methods in Fig. 7(b) to (l) for the case of the dark saturation phenomenon.

The result of Fig. 7(c) by the GHE is saturated at the boundary between the mountain and the sky. The reason for such problems can be inferred from the histogram in Fig. 7(c). In the low dynamic image, the difference of pixel brightness between the sky and mountain is small. Also, in a histogram with a low FF index, like the histogram in Fig. 7(c), it is difficult to distinguish between mountains and sky boundaries. In Fig. 7(e) and (f), the contrast ratio is very high, but the noise is dramatically pronounced in the entire image including the sky. The histograms in Fig. 7(e) and (f) are expressed with a high FF factor, but the distribution of histograms shows a big difference in comparison to the GT image. Fig. 7(g) and (h) are stretched around the mean brightness of the input image, but the effect is low. Fig. 7(i) has less noise and better histogram results, but there is white saturation that blurs the boundary between mountains and sky. Fig. 7(j) shows excellent performance when visually evaluating the quality of overall image areas. However, the FF value is low, so there are low contrast parts of the black and white representation. Fig. 7(k) shows the intermediate result between (j) and (l). The white and black saturation problems are attenuated a bit more, but the contrast resolution was low due to the low FF.

In Fig. 8, we show the experimental results when white saturation occurs. The results in Fig. 8(c), (e), (f) and (l) same methods are used as in Fig. 7. The results of other methods show different image quality of black saturated and white saturated images. This is especially true for methods used in Fig. 8(i) and (j), which perform well in the black saturation test in Fig. 7, but return degraded image for the cases with white saturation conditions.

On the other hand, the proposed method shows robust quality in various experimental conditions for black and white
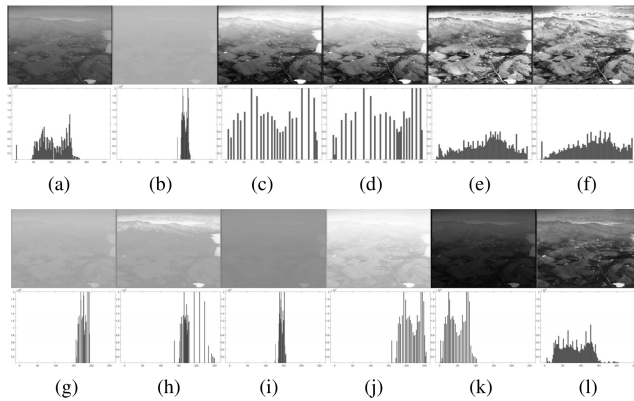
**FIGURE 8.** *IRST-UAV* white low-dynamic image (upper rows: results of images, lower rows: results of histogram [x-axis: levels of intensity, y-axis: number of pixels]) (a) GT, (b) Input, (c) GHE, (d) BBHE, (e) CLAHE, (f) IHE, (g) DSIHE, (h) BPDHE, (i) SVD-DWT, (j) AGCWD, (k) CegaHE, (l) Proposed.

saturated images. Furthermore, the results contain low noise levels, high histogram fill factor and high similarity to the original image with high contrast enhancement performance.

## B. VISUAL ASSESSMENT OF THE SATELLITE DATASET

Satellites are equipped with electro-optical infrared (EO/IR) imaging systems using multi-wavelength sensors to observe various terrains and oceans and analyze atmospheric phenomena in detail. The images in Fig. 9 and 10 are obtained from the satellite EO/IR imaging systems of the Landsat-8 satellite [26]. Fig. 9(a) shows near-infrared (NIR, 0.845 - 0.885 $\mu$m) of the fifth wavelength-band (*Wave-05*) image, and Fig. 10(a) shows images acquired with long wavelength infrared (LWIR, 10.30 - 11.30 $\mu$m) of the tenth wavelength-band (*Wave-10*). As can be seen from the two GT images, even when the surface of the earth with the same heat source is photographed, use of NIR can result in the dark saturation and use of LWIR can produce white saturated images.

Since the GT of NIR image shown in Fig. 9(a), already shows considerable low dynamic characteristics, we experimented with the input image as shown in Fig. 9(b). The LWIR image in Fig. 10(a) is used as an input image by applying a bias to obtain a white-saturated image as shown in Fig. 10(b). As shown in Fig. 9(c) and Fig. 10(d), the two images show low contrast resolution due to the poor fill factor of the histogram. Fig. 10(e) and (f) show high contrast resolutions but the noise levels in the resulting images are emphasized. Additionally, the part of the image with the black sea is changed to gray and the image was distorted. In Fig. 10(g) and (h), a lot of low dynamic components are still presented. Fig. 10(i) shows insufficient contrast stretching, which is particularly vulnerable to white saturation. Fig. 9(j) shows good results for black saturated images, but Fig. 10(j) shows that method's stretching effect is deteriorated in the case of white saturated images. Fig. 9(k) and the Fig. 10(k) show that method expands the contrast to the appropriate level, but the fill factor is low and both results are biased in the dark region. On the other hand, Fig. 9(l) and Fig. 10(l) show robust
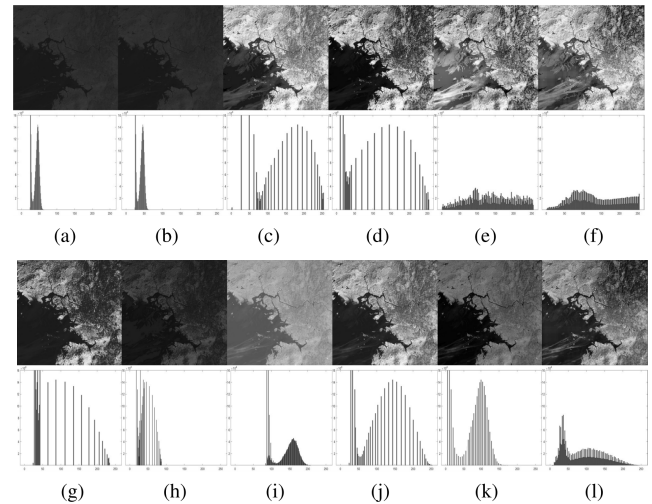


**FIGURE 9.** *Wave-05* dark low-dynamic image (upper rows: results of images, lower rows: results of histogram [x-axis: levels of intensity, y-axis: number of pixels]) (a) GT, (b) Input, (c) GHE, (d) BBHE, (e) CLAHE, (f) IHE, (g) DSIHE, (h) BPDHE, (i) SVD-DWT, (j) AGCWD, (k) CegaHE, (l) Proposed.



**FIGURE 10.** *Wave-10* white low-dynamic image (upper rows: results of images, lower rows: results of histogram [x-axis: levels of intensity, y-axis: number of pixels]) (a) GT, (b) Input, (c) GHE, (d) BBHE, (e) CLAHE, (f) IHE, (g) DSIHE, (h) BPDHE, (i) SVD-DWT, (j) AGCWD, (k) CegaHE, (l) Proposed.
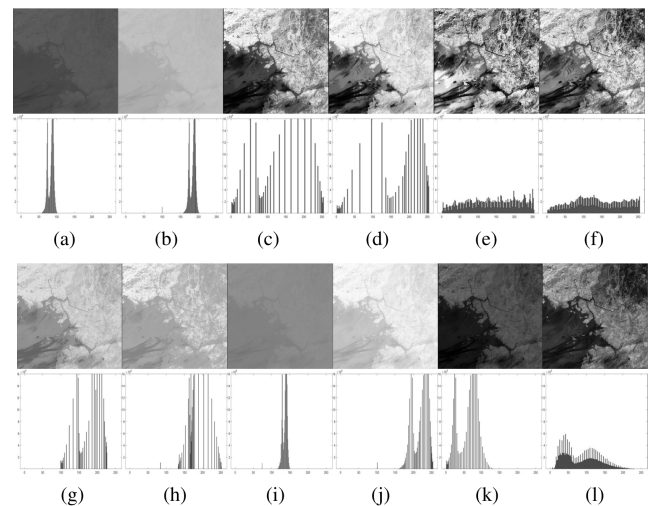
enhancement results for both dark and white saturation with high fill factor. The resulting images have the highest contrast resolution.

## C. VISUAL ASSESSMENT OF THE SURVEILLANCE DATASET

Images similar to the ones in Fig. 11(a) are obtained with surveillance products including IRST. It is necessary to observe all the image components such as the shape of the road around the target and surrounding objects simultaneously with the detection of the target. Actually, the details of background contrast affect the capability of finding the objects using human eyes, tracking algorithms and automatic detection algorithms for conventional or deep-learning methods [27].
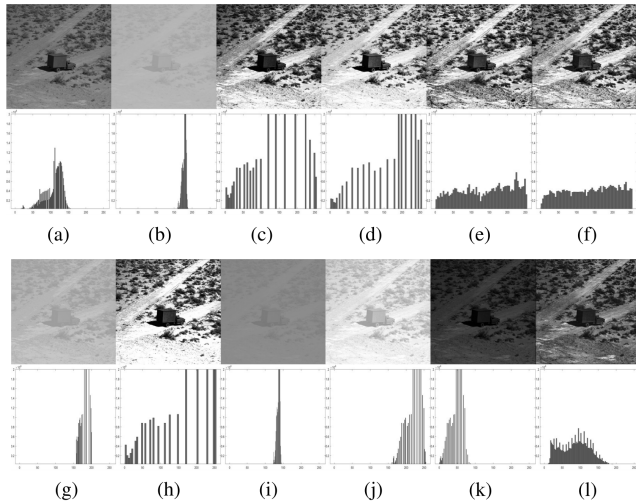
**FIGURE 11.** *Truck* white low-dynamic image (upper rows: results of images, lower rows: results of histogram [x-axis: levels of intensity, y-axis: number of pixels]) (a) GT, (b) Input, (c) GHE, (d) BBHE, (e) CLAHE, (f) IHE, (g) DSIHE, (h) BPDHE, (i) SVD-DWT, (j) AGCWD, (k) CegaHE, (l) Proposed.



**FIGURE 12.** *An eye* white low-dynamic image (upper rows: results of images, lower rows: results of histogram [x-axis: levels of intensity, y-axis: number of pixels]) (a) GT, (b) Input, (c) GHE, (d) BBHE, (e) CLAHE, (f) IHE, (g) DSIHE, (h) BPDHE, (i) SVD-DWT, (j) AGCWD, (k) CegaHE, (l) Proposed.

Following, the input image in Fig. 11(b), results show white saturation occurs in images of all methods except in Fig. 11(k). The result in Fig. 11(k) does not show white saturation, but it shows a low dynamic image which is biased to the dark area. The resulting image of the proposed method shown in Fig. 11(l) displays the truck and the background are preserved well without dark and white saturation.

### D. VISUAL ASSESSMENT OF AN EYE DATASET

Fig. 12(a) shows a retinal optical coherence tomography image of an eye used for ophthalmological diagnosis. It is very important to carefully inspect all areas of the image and to find any abnormal cells or blood vessels for defining accurate diagnosis.

In Fig. 12(e) and (f), the features of the blood vessels are very clear, but it is difficult to diagnose any abnormal tissue in the boundary areas due to the partial white saturation. On the other hand, the method proposed in Fig. 12(l) does not saturate the background and object components, and the histogram resolution for all image area is high.

### E. VISUAL ASSESSMENT OF THE HAZY DATASET

In previous sections, we showed that the proposed method can be applied to IR sensor images, security images, medical images, and a wide range of monochrome images like IR or grayscale. It was also shown that the proposed method can be used for performance improvement. We have also attempted to evaluate whether the proposed method can be used to solve saturation problems in conditions such as fog and high illumination in color images. Fig. 13(a) is a representative low-dynamic color image including fog, where we compare the performance of the 10 methods in the same way as in the previous experiments. Using each method, the input image shown in Fig. 13(b) can be improved as
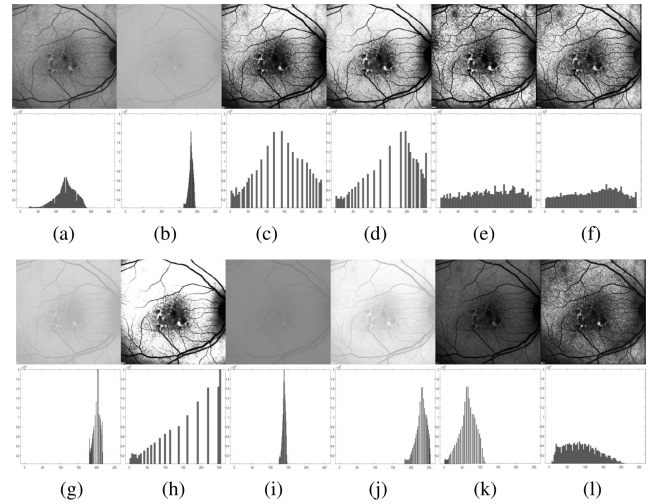


**FIGURE 13.** *Hazy* white low-dynamic image (upper rows: results of images, lower rows: results of histogram [x-axis: levels of intensity, y-axis: number of pixels]) (a) GT, (b) Input, (c) GHE, (d) BBHE, (e) CLAHE, (f) IHE, (g) DSIHE, (h) BPDHE, (i) SVD-DWT, (j) AGCWD, (k) CegaHE, (l) Proposed.
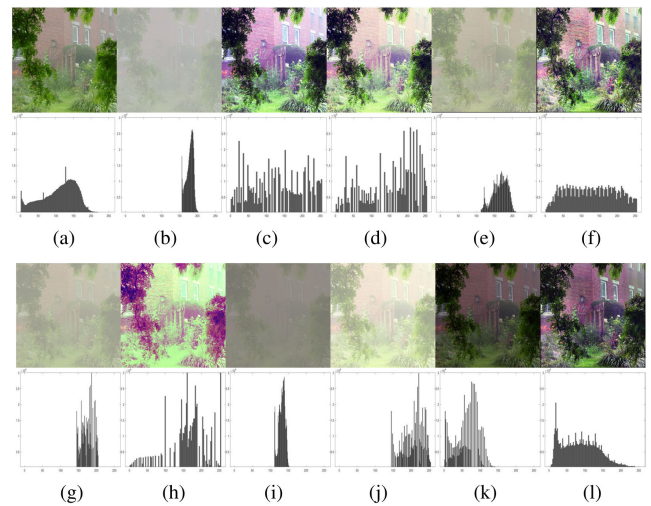
shown in Fig. 13(c) to (l). In this case, Fig. 13(c) and (f) show good performance, but the glare of many of lights is visible in the visual evaluation. The resulting image of the proposed method shown in Fig. 13(l) expresses an adequate amount of comfortable light and high contrast resolution and at the same time eliminates the hazy areas.

### F. REAL-TIME VIDEO SEQUENCES

It is very important to improve the performance of real-time IRST products at the same time as further develop countermeasures. It is necessary to confirm the result of the improvement of the contrast performance of continuous images as a result of applying the method to the actual product. For this experiment, we use a real-time video dataset with reduced
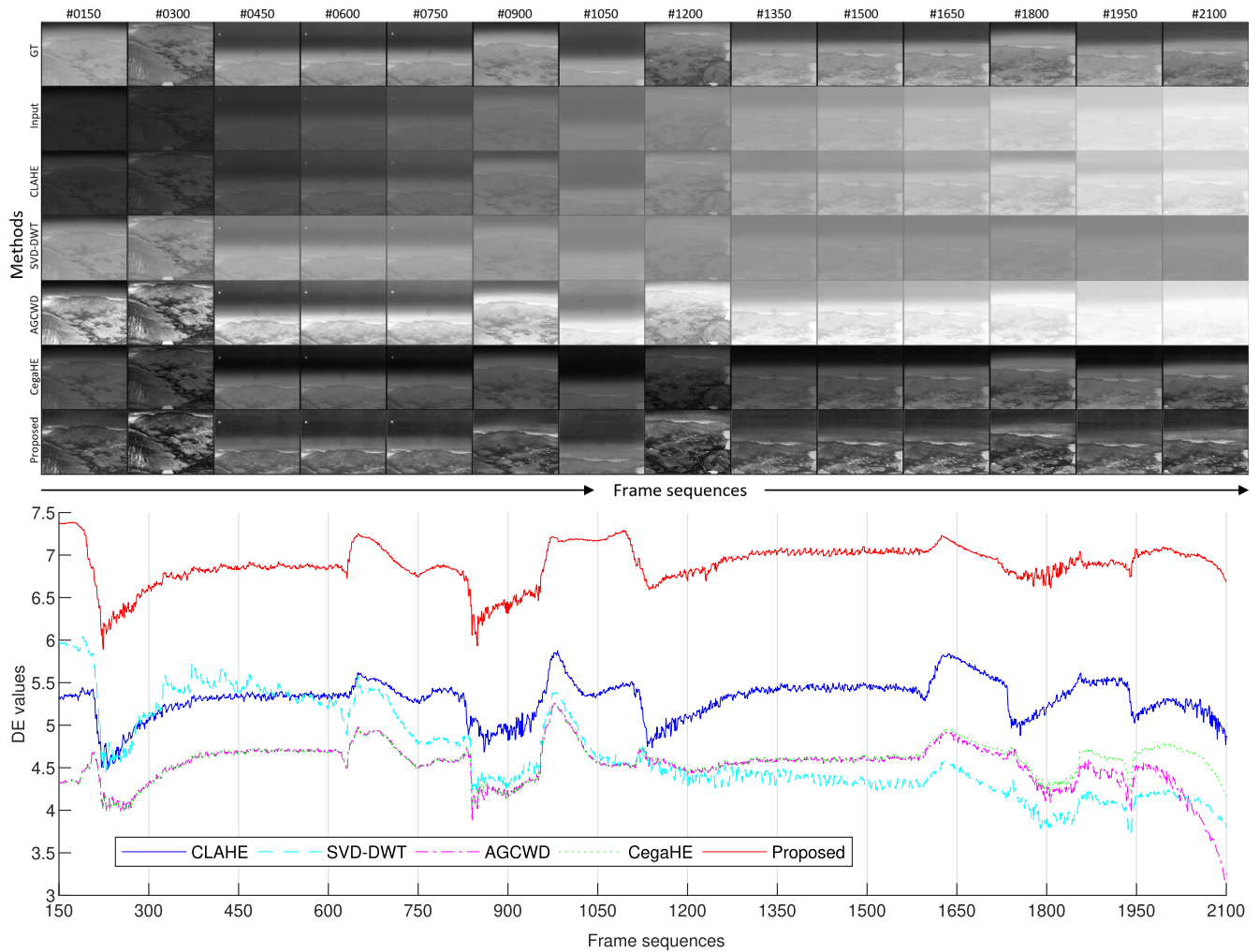
**FIGURE 14.** Real time video sequences of *IRST-UAV* dataset (#0150~#2100).

image dynamics characteristics by changing the saturation from white to dark. The results for every 150th frame of the sequence are shown in Fig. 14.

Using the best performing five methods in the visual assessment from Fig. 7 to 13, comparison results were obtained from video images. The proposed method shows the most stable contrast enhancement results in the visual evaluation of continuous images. In order to quantitatively measure the improvement ratio of the contrast, the improvement ratio of the contrast of every single video frame according to five different methods is measured using the contrast index. The quantitative index for measurement of the contrast improvement is used as the discrete entropy (DE) index, which is calculated as:

$$DE = -\sum_{i=1}^{j} p(x_i) \times log_2 p(x_i) \quad (16)$$

In cases of frames #0150 and #0300, the AGCWD also shows good results. However, the DE index values are significantly lower than for the proposed method. This is true due to the same reason that occurs in the experimental results

in Fig. 7(j). The AGCWD method stretches the contrast to the maximum width in image levels. However, since the fill factor of the histogram is low, the contrast resolution is not at a high level. Observing the actual image in detail confirms that there is a problem with finding and recognizing SML region. Also, as shown in the video sequence after #1200, the performance of contrast enhancement using CLAHE, SVD-DWT, and AGCWD methods decrease significantly in white saturation.

In contrast, the overall DE values of the CLAHE method are robust from the first to the final frame. This shows the same characteristics as shown in Fig. 7(e) and Fig 8(e). The proposed method also shows robust performance throughout all video frames in dark and white saturation situations. It shows the higher DE value than CLAHE and clearer results than other methods.

## V. QUANTITATIVE MEASUREMENTS
### A. METRICS OF MEASUREMENT INDEXES
The quantitative measurement related to the improvement of the image contrast is the DE index as shown in the

graph in Fig. 14 for a video example. Although the proposed method showed high DE measurement results, in some cases, CLAHE or IHE methods outperform the proposed method as shown in Fig. 15(a), which shows the DE results for individual images. However, the higher DE results cannot be always recognized as better performance. This is because the image with a good contrast improvement results with a high DE can contain a lot of noise compared to the original or can take longer calculation times.

Therefore, in order to evaluate images using a quantitative measure, it is necessary to minimize the noise levels with DE, the image distortion in comparison with the original image, and the calculation times. The conventional image improvement studies are also use various noise improvement indexes with contrast enhancement indexes [28], [29]. We use peak signal to noise ratio (PSNR), structural similarity (SSIM), and root mean square error (RMSE) considering the distortion and the noise-related measurement indexes, calculated with equations 17 to 19.

$$\text{PSNR}(I_x, I_y) = 10 \times \log_{10}\left(\frac{I_{max}^2}{\text{MSE}(I_y, I_x)}\right), \quad (17)$$

where $I_x$ is the original GT image, and $I_y$ is the output image. $I_{max}$ is the max dynamic range of input and output images. $I_{max}$ is 255 for 8-bit image. The MSE is the mean square error of the output image in comparison with the original image.

$$\text{SSIM}(I_x, I_y) = \frac{(2\mu_x\mu_y + C_1)(2\sigma_{xy} + C_2)}{(\mu_x^2 + \mu_y^2 + C_1)(\sigma_x^2 + \sigma_y^2 + C_2)}, \quad (18)$$

where $\mu_x$ and $\mu_y$ are the average values of input and output images. $\sigma_x$ and $\sigma_y$ are the variances of input and output images. $C_1 = k_1 I_{max}^2$ and $C_2 = k_2 I_{max}^2$. $k_1 = 0.01$, $k_2 = 0.03$.

$$\text{RMSE} = \frac{1}{MN}\sum_{i=1}^{M}\sum_{j=1}^{N}(I_{\text{out}} - I_{\text{gt}})^2. \quad (19)$$

### B. ASSESSMENT USING INDIVIDUAL INDEXES

Experiments are performed using many different images acquired using different sensors and showing different scenes. We performed experiments with datasets *IRST* (12 images), *Remote-sensing* (10 images), *Surveillance* (5 images), *General-grayscale* (7 images), *RGB* (8 images). All of the visual assessment results for every single image are attached in the supplemental materials. Fig. 15(a) shows results of 10 different methods using *IRST* (12 images) experimental images. Five graphs in Fig. 15(a) are measurement results for calculation time(T), entropy(E), PSNR(P), SSIM(S), RMSE(R), respectively from the top. The 12 experimental images show slightly different performance measurement results and Fig. 15(b) shows the average of all results in Fig. 15(a).

The lower T and R indexes mean better performance, higher E, P, and S mean better performance. Using the proposed method, the quantitative measurement results of the IRST experimental dataset showed good performance for all
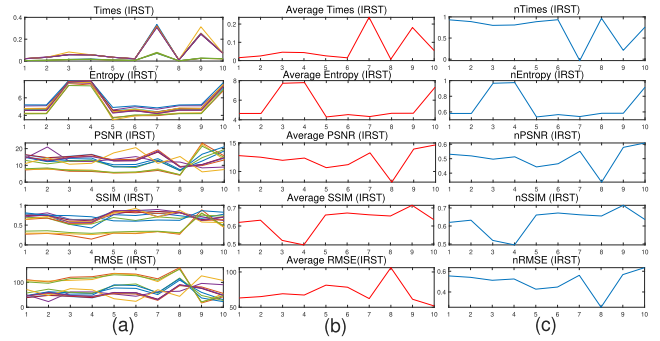


**FIGURE 15.** Quantitative measurement using *IRST* dataset (12 images), [x-axis: methods(1:GHE, 2:BBHE, 3:CLAHE, 4:IHE, 5:DSIHE, 6:BPDHE, 7:SVD-DWT, 8:AGCWD, 9:CegaHE, 10:Proposed), y-axis: index values], (a) individual TEPSR, (b) average TEPSR, (c) normalized TEPSR.

but the T index of SVD-DWT and CegaHE method. The E index shows that the proposed method outperforms others, followed by IHE, and CLAHE. In addition, SVD-DWT and the proposed method show good performance for P, S, R due to low noise levels.

Fig. 16 and Fig. 17 show the measurement results for four more datasets: *Remote-sensing*, *Surveillance*, *General-grayscale*, and *General-RGB*.

### C. INTEGRATED ASSESSMENT USING NORMALIZED TEPSR

We have used time, entropy, signal-to-noise ratio, structural similarity, and the root mean square error as individual indexes for quantitative measurement. For image improvement evaluation, several factors should be considered, and we use the normalized measurement index as an evaluation technique for comprehensive performance evaluation.

The purpose of this is to normalize each index and to evaluate when an image is improved with the integrated indicator. As an integrated index, normalized T, E, P, S, R (nTEPSR) is calculated as:

$$\text{nTEPSR} = \frac{1}{N}[(1 - \frac{T_i}{T_{\max} - T_{\min}}) + \frac{E_i}{Bits}$$
$$+ \frac{P_i}{20\log_{10}L} + S_i + (1 - \frac{R_i}{1 - R_{\max} - R_{\min}})] \quad (20)$$

With the nTEPSR measurement graphs shown in Fig. 15 to 17, we can confirm the advantages and disadvantages of the ten compared methods. For example, compared with 1:GHE, 4:IHE shows the best contrast expansion performance and faster speed, however, the output is very noisy. 7:SVD-DWT is slow, but its output is less noisy. 8:AGCWD is fast, but the output is noisy and has low contrast expansion performance. 9:CegaHE shows the results of medium calculation speed and very low noise levels, but poor contrast in the output images. 10:Proposed method has lower noise levels and good contrast ratio in output images, allows fast calculation and retains robust performance for all testing datasets.
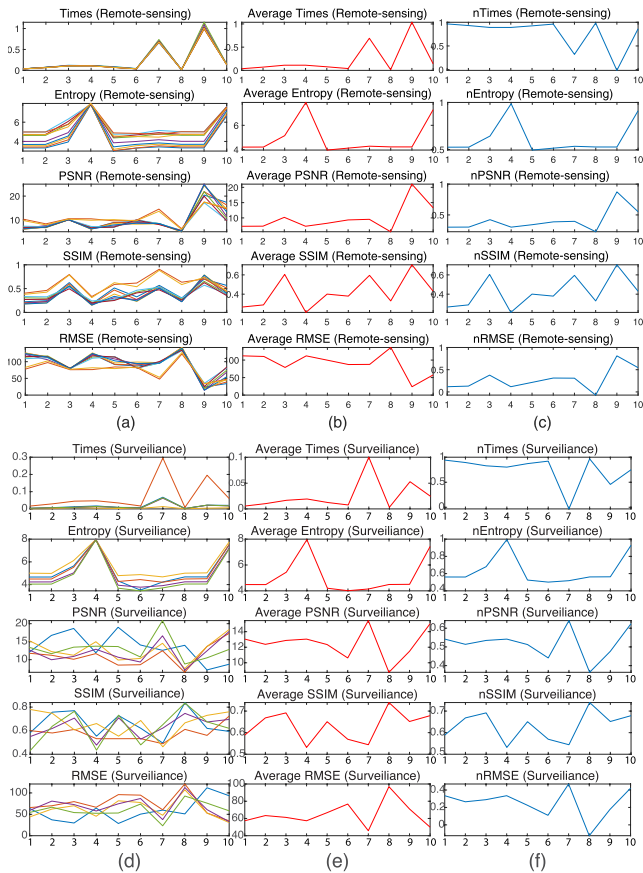
**FIGURE 16.** Quantitative measurement using *Remote-sensing* and *Surveillance* datasets, [x-axis: methods(1:GHE, 2:BBHE, 3:CLAHE, 4:IHE, 5:DSIHE, 6:BPDHE, 7:SVD-DWT, 8:AGCWD, 9:CegaHE, 10:Proposed), y-axis: index values], (a) individual TEPSR, (b) average TEPSR, (c) normalized TEPSR of *Remote-sensing*, (d) individual TEPSR, (e) average TEPSR, (f) normalized TEPSR of *Surveillance* datasets.



**FIGURE 17.** Quantitative measurement using *Grayscale* and *RGB* datasets. [x-axis: methods(1:GHE, 2:BBHE, 3:CLAHE, 4:IHE, 5:DSIHE, 6:BPDHE, 7:SVD-DWT, 8:AGCWD, 9:CegaHE, 10:Proposed), y-axis: index values], (a) individual TEPSR, (b) average TEPSR, (c) normalized TEPSR of *Grayscale*, (d) individual TEPSR, (e) average TEPSR, (f) normalized TEPSR of *RGB* datasets.

Table 3 shows summarized comparison results using the integrated nTEPSR index measured in images in Fig. 15 to 17 from datasets *IRST*, *Remote-sensing*, *General-grayscale*, and *General-RGB* test images.

The five top rows in Table 3 show the measurement results of nTEPSR for each dataset. The average is the mean value for each method for the five different datasets. The variation of nTEPSR value refers to the maximum variations between the best and the worst result of nTEPSR for the five datasets. The bold text highlights the highest and the second highest performance results.

The proposed method shows the highest performance values for each dataset and their averages. Since the variation is small, the image quality improvement performance is robust to the change of the image data. For example, the results show that the proposed method outperforms other methods with an average rank score of 0.73, followed by IHE and CLAHE methods with rank scores of 0.67 and 0.63 respectively. The MV of the proposed method is 0.08, and SVD-DWT method shows the value of 0.07. This means the performance of SVD-DWT is more constant, but overall lower than that of the
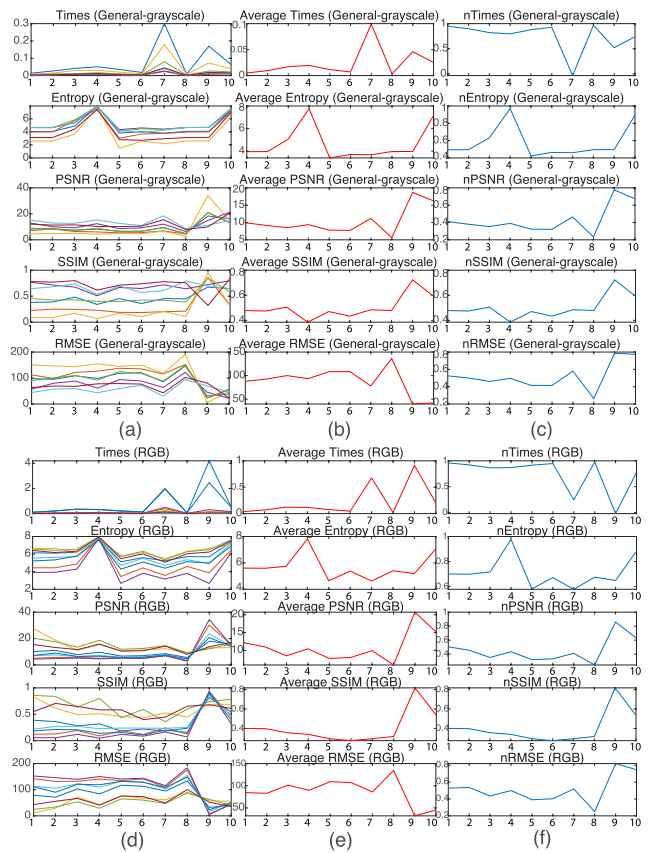
proposed method. Additionally, Table 3 shows the FPS values according to the running time analysis result. All methods were run on the same workstation (a single Intel CPU i7-7700 3.6GHz 32GB RAM) using MATLAB. The AGCWD and GHE methods have strengths of the computational speed. On the other hand, the SVD-DWT and CegaHE show very slow speed. The proposed method shows a moderate level of speed, and it is measured 2.65 times faster (29 FPS) by the C++ script conversion. It is expected to be capable of real-time operation in the embedded systems.

Fig. 18(a) is a graphical representations of results from Table 3, and shows the overall score by averaging the nTEPSR results for each datasets. Fig. 18(b) shows the maximum variation of each methods. In Fig. 18(a) and Fig. 18(b), according to the result of comprehensive graphical analysis, the conventional IHE method has the second highest performance next to the proposed method [23]. However, as shown in the raw data measurement results in Fig. 15 to Fig. 16, IHE is not as good as other methods in terms of noise performance. The proposed introduces the lesser amount of noise into the output images than most of other methods.

**TABLE 3.** Quantitative measurement using the nTEPSR index and an analysis of running time.

| Datasets | GHE | BBHE | CLAHE | IHE | DSIHE | BPDHE | SVD-DWT | AGCWD | CegaHE | Proposed |
|---|---|---|---|---|---|---|---|---|---|---|
| *IRST* | 0.64 | 0.63 | **0.66** | **0.66** | 0.59 | 0.62 | 0.46 | 0.56 | 0.53 | **0.71** |
| *Remote-sensing* | 0.57 | 0.57 | 0.67 | **0.70** | 0.58 | 0.61 | 0.43 | 0.56 | 0.44 | **0.76** |
| *Surveillance* | 0.59 | 0.58 | 0.60 | **0.64** | 0.56 | 0.51 | 0.43 | 0.50 | 0.46 | **0.68** |
| *General-grayscale* | 0.57 | 0.55 | 0.55 | 0.61 | 0.50 | 0.51 | 0.39 | 0.49 | **0.66** | **0.73** |
| *General-RGB* | 0.71 | 0.69 | 0.65 | **0.75** | 0.61 | 0.65 | 0.41 | 0.64 | 0.48 | **0.76** |
| **Average nTEPSR** | 0.62 | 0.60 | 0.63 | **0.67** | 0.57 | 0.58 | 0.42 | 0.55 | 0.51 | **0.73** |
| **Variation nTEPSR** | 0.14 | 0.14 | 0.12 | 0.14 | 0.11 | 0.14 | **0.07** | 0.15 | 0.22 | **0.08** |
| **Running time (msec)** | **20** | 37 | 62 | 62 | 41 | 23 | 361 | **10** | 446 | 89 |
| **FPS** | **50.9** | 26.9 | 16.0 | 16.0 | 24.6 | 43.0 | 2.7 | **99.7** | 2.2 | 11.2 |
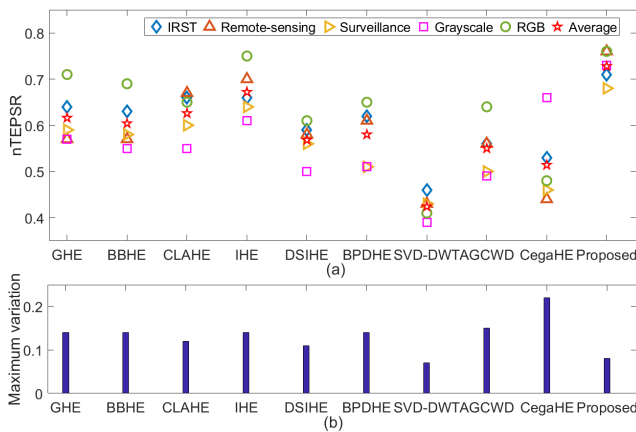


**FIGURE 18.** Measurement results of average normalized TEPSR. [x-axis: methods, y-axis: integrated measurement values], (a) nTEPSR of each dataset with an average (b) maximum variation of nTEPSR.

## VI. CONCLUSION

In this study, we proposed a new contrast enhancement method for low dynamic images acquired by IRST, EO/IR, and grayscale or RGB vision sensor systems. The motivation of the proposed method is 3D histogram analysis and a three-step ASNU process for improving image quality after CF. For the first step in ASNU, the IDH reduces channel noise. In the second step, the CDF-reshaping process is used to suppress non-uniformity in images. In the third step, a dark area restoration process recovers dark pixel levels and reduces the noise at the same time.

Compared with conventional methods, not only does the proposed method to show the high contrast enhancement effect in black and white saturation simultaneously, but also allows real-time operation capable speed and contains low noise levels in the resulting images. As a result of this study, it is expected that the detection and recognition distance can be extended by applying the gated mode image processing for use with IRST and EO/IR systems in the haze or low-visibility environment.

As part of future work, we have a plan to apply the proposed method for improvement of detection performance of a supervised deep learning algorithm as an advanced training

data generation technique and pre-processing step for object detection in the inference process.

## REFERENCES

[1] B. Kim, M. Kim, and Y. Chae, "Background registration-based adaptive noise filtering of LWIR/MWIR imaging sensors for UAV applications," *Sensors*, vol. 18, no. 2, p. 60, Dec. 2017.

[2] P. A. Coelho, J. E. Tapia, F. Pérez, S. N. Torres, and C. Saavedra, "Infrared light field imaging system free of fixed-pattern noise," *Sci. Rep.*, vol. 7, no. 1, 2017, Art. no. 13040.

[3] V. John, S. Mita, Z. Liu, and B. Qi, "Pedestrian detection in thermal images using adaptive fuzzy C-means clustering and convolutional neural networks," in *Proc. 14th IAPR Int. Conf. Mach. Vis. Appl. (MVA)*, May 2015, pp. 246–249.

[4] J. Redmon, S. Divvala, R. Girshick, and A. Farhadi, "You only look once: Unified, real-time object detection," in *Proc. IEEE Conf. Comput. Vis. Pattern Recognit. (CVPR)*, Jun. 2016, pp. 779–788.

[5] M. Kristan, J. Matas, A. Leonardis, T. Vojíř, R. Pflugfelder, G. Fernandez, G. Nebehay, F. Porikli, and L. Čehovin, "A novel performance evaluation methodology for single-target trackers," *IEEE Trans. Pattern Anal. Mach. Intell.*, vol. 38, no. 11, pp. 2137–2155, Nov. 2016.

[6] A. Lukezic, T. Vojir, L. C. Zajc, J. Matas, and M. Kristan, "Discriminative correlation filter with channel and spatial reliability," in *Proc. IEEE Conf. Comput. Vis. Pattern Recognit. (CVPR)*, Jul. 2017, pp. 6309–6318.

[7] A. Lukezic, L. C. Zajc, and M. Kristan, "Deformable parts correlation filters for robust visual tracking," *IEEE Trans. Cybern.*, vol. 48, no. 6, pp. 1849–1861, Jun. 2018.

[8] A. Lukezic, U. Kart, J. Kapyla, A. Durmush, J.-K. Kamarainen, J. Matas, and M. Kristan, "CDTB: A color and depth visual object tracking dataset and benchmark," in *Proc. IEEE Int. Conf. Comput. Vis.*, Oct. 2019, pp. 10013–10022.

[9] M. Wan, G. Gu, W. Qian, K. Ren, X. Maldague, and Q. Chen, "Unmanned aerial vehicle video-based target tracking algorithm using sparse representation," *IEEE Internet Things J.*, vol. 6, no. 6, pp. 9689–9706, Dec. 2019.

[10] R. C. Gonzalez and R. E. Woods, *Digital Image Processing*. New York, NY, USA: Person, 2018.

[11] Q. Wang and R. Ward, "Fast image/video contrast enhancement based on weighted Thresholded histogram equalization," *IEEE Trans. Consum. Electron.*, vol. 53, no. 2, pp. 757–764, May 2007.

[12] R. Vadivambal and D. S. Jayas, "Applications of thermal imaging in agriculture and food industry—A review," *Food and Bioprocess Technol.*, vol. 4, no. 2, pp. 186–199, Feb. 2011.

[13] M. Diakides, J. D. Bronzino, and D. R. Peterson, *Medical Infrared Imaging: Principles and Practices*. Boca Raton, FL, USA: CRC Press, 2012.

[14] M. Vollmer and M. Klaus-Peter, *Infrared Thermal Imaging: Fundamentals, Research and Applications*. Hoboken, NJ, USA: Wiley, 2017.

[15] Y.-T. Kim, "Contrast enhancement using brightness preserving bi-histogram equalization," *IEEE Trans. Consum. Electron.*, vol. 43, no. 1, pp. 1–8, Feb. 1997.

[16] M. Wan, G. Gu, W. Qian, K. Ren, Q. Chen, and X. Maldague, "Particle swarm optimization-based local entropy weighted histogram equalization for infrared image enhancement," *Infr. Phys. Technol.*, vol. 91, pp. 164–181, Jun. 2018.

[17] G. Yadav, S. Maheshwari, and A. Agarwal, "Contrast limited adaptive histogram equalization based enhancement for real time video system," in *Proc. Int. Conf. Adv. Comput., Commun. Informat. (ICACCI)*, Sep. 2014, pp. 2392–2397.

[18] Y. Wang, Q. Chen, and B. Zhang, "Image enhancement based on equal area dualistic sub-image histogram equalization method," *IEEE Trans. Consum. Electron.*, vol. 45, no. 1, pp. 68–75, Feb. 1999.

[19] H. Ibrahim and N. P. Kong, "Brightness preserving dynamic histogram equalization for image contrast enhancement," *IEEE Trans. Consum. Electron.*, vol. 53, no. 4, pp. 1752–1758, Nov. 2007.

[20] H. Demirel, C. Ozcinar, and G. Anbarjafari, "Satellite image contrast enhancement using discrete wavelet transform and singular value decomposition," *IEEE Geosci. Remote Sens. Lett.*, vol. 7, no. 2, pp. 333–337, Apr. 2010.

[21] S.-C. Huang, F.-C. Cheng, and Y.-S. Chiu, "Efficient contrast enhancement using adaptive gamma correction with weighting distribution," *IEEE Trans. Image Process.*, vol. 22, no. 3, pp. 1032–1041, Mar. 2013.

[22] C.-C. Chiu and C.-C. Ting, "Contrast enhancement algorithm based on gap adjustment for histogram equalization," *Sensors*, vol. 16, no. 6, p. 936, Jun. 2016.

[23] B. H. Kim and M. Y. Kim, "Anti-saturation and contrast enhancement technique using interlaced histogram equalization (IHE) for improving target detection performance of EO/IR images," in *Proc. 17th Int. Conf. Control, Automat. Syst. (ICCAS)*, Oct. 2017, pp. 1692–1695.

[24] B. Wang, W. Li, W. Yang, and Q. Liao, "Illumination normalization based on Weber's Law with application to face recognition," *IEEE Signal Process. Lett.*, vol. 18, no. 8, pp. 462–465, Aug. 2011.

[25] S. Rahman, M. M. Rahman, M. Abdullah-Al-Wadud, G. D. Al-Quaderi, and M. Shoyaib, "An adaptive gamma correction for image enhancement," *EURASIP J. Image Video Process.*, vol. 2016, no. 1, p. 35, 2016.

[26] USGS. (2019). *Geographic Information Systems Dataset, Landset8 Satellite*. Accessed: Mar. 7, 2019. [Online]. Available: https://www.usgs.gov/faqs/what-are-band-designations-landsatsatellites-0?qt-news-science-products=7#qt-news-science-products

[27] M. Fiaz, A. Mahmood, S. Javed, and S. K. Jung, "Handcrafted and deep trackers: A review of recent object tracking approaches," *ACM Comput. Surv.*, vol. 52, no. 2, 2019, Art. no. 43.

[28] P.-J. Liu, S.-J. Horng, J.-S. Lin, and T. Li, "Contrast in haze removal: Configurable contrast enhancement model based on dark channel prior," *IEEE Trans. Image Process.*, vol. 28, no. 5, pp. 2212–2227, May 2019.

[29] S. Salazar-Colores, E. Cabal-Yepez, J. M. Ramos-Arreguin, G. Botella, L. M. Ledesma-Carrillo, and S. Ledesma, "A fast image Dehazing algorithm using morphological reconstruction," *IEEE Trans. Image Process.*, vol. 28, no. 5, pp. 2357–2366, May 2019.

**CIRIL BOHAK** received the Ph.D. degree from the Faculty of Computer and Information Science, University of Ljubljana, in 2016.

He is currently a Teaching Assistant with the Faculty of Computer and Information Science, University of Ljubljana. He is also teaching courses computer graphics, game technology, and computer aided design. His researches include computer graphics, data visualization, human-computer interaction, music information retrieval, gamification, E-learning, and game technology. He is also one of the Founding Members of the Slovenian HCI Community.
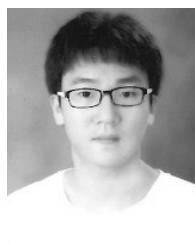
**KI HOON KWON** received the M.S. degree from the School of Electronic Engineering, Kyungpook National University (KNU), Daegu, South Korea, where he is currently pursuing the Ph.D. degree.

He has authored or coauthored more than five articles in journals and conferences. His current research interests include image resolution enhancement, integral imaging microscopy, infrared image object detection, and human intention estimation systems.

**MIN YOUNG KIM** received the B.S., M.S., and Ph.D. degrees from the Korea Advanced Institute of Science and Technology, South Korea, in 1996, 1998, and 2004, respectively. He was a Senior Researcher with Mirae Corporation, from 2004 to 2005, and a Chief Research Engineer with Koh Young Corporation, from 2005 to 2009, in the research field of artificial vision systems for intelligent machines and robots. Since 2009, he has been an Assistant Professor with the School of Electrical Engineering and Computer Science, Kyungpook National University. He was a Visiting Associate Professor with the Department of Electrical and Computer Engineering and School of Medicine, Johns Hopkins University, from 2014 to 2016. He is currently an Associate Professor with the School of Electronics Engineering, Kyungpook National University, the Deputy Director of the KNU-LG Convergence Research Center, and the Director of the Research Center for Neurosurgical Robotic Systems. His research interest is the visual intelligence for robotic perception and recognition of autonomous unmanned ground and aerial vehicles.

**BYEONG HAK KIM** received the M.S. degree from the School of Electronic Engineering, Kyungpook National University (KNU), Daegu, South Korea, where he is currently pursuing the Ph.D. degree. He is also a Senior Engineer with the Department of Optronics, Hanwha Systems Company, Gumi, South Korea. His current research interests include infrared image enhancement, visual object tracking, deep-learning object auto detection, 3-D laser radar, and counter drone systems.

• • •